Nanoscale

PAPER

View Article Online
View Journal | View Issue

Cite this: *Nanoscale*, 2024, **16**, 15713

Magnetic clusters as efficient EY-like spin-scattering centres in graphene†

Wout Keijers, [a] Ramasamy Murugesan, [b] Guillaume Libeert, [a] Bart Raes, [c] Steven Brems, [c] Stefan De Gendt, [c] Michel Houssa, [b] Ewald Janssens *[a] and Joris Van de Vondel *[a]

Received 4th April 2024,
Accepted 14th July 2024

DOI: 10.1039/d4nr01478b

rsc.li/nanoscale

The spin scattering induced by magnetic adsorbates on graphene was studied using a combination of transport measurements on a graphene field effect transistor decorated with atomically precise nickel clusters and first principles calculations. A comparative study before and after deposition of Ni_4 clusters unambiguously corroborated the contribution of the added scatterers. An investigation of the spin scattering parameters as a function of the applied voltage indicated a cluster-induced Elliot–Yafet like spin scattering mechanism. Density functional theory calculations were used in combination with a tight-binding model to quantify the strength of the spin–orbit coupling terms induced by the adsorbed clusters.

1 Introduction

Controlled doping by impurities can provide semiconducting materials with the desired properties. In the case of two-dimensional materials, the adsorption of metal atoms and nanoparticles offers a similar platform to extend functionalities. For example, to transform graphene into a spin active material, a strong Rashba spin–orbit coupling can be induced by the proximity effect. Transition metal dichalcogenides (TMDs) and adatoms have the potential to enhance spin–orbit coupling (SOC),[1–3] thereby inducing spin anisotropy[4–7] and robust quantum spin Hall states, enabling gate manipulation of spin transport and the conversion of electrical currents into spin currents *via* the spin Hall effect (SHE) or *vice versa* (iSHE).[8–11] However, fundamental questions remain on the spin relaxation mechanisms in graphene. Both experimental and theoretical studies dealing with the influence of impurities and adatoms on spin scattering yield contradictory results on the dominant spin scattering mechanism.[12–16] In a recent proof-of-principle experiment, we investigated the spin transport parameters of graphene spin valves decorated with soft-landed, size-selected, few-atom Au_n clusters.[17] A study as a function of cluster density allowed the derivation of cluster-size dependent spin and momentum scattering times.

Exploiting the material flexibility of cluster beam deposition, we redirect our attention to magnetic clusters to identify their impact on the spin transport of the hybrid structure. We focus on nickel clusters due to their relatively high intrinsic magnetic moments,[18] which are predicted to not be completely quenched when adsorbed on perfect graphene.[19] In order to select the most appropriate cluster size, the electronic structure of Ni_n (n = 2–5) clusters adsorbed on graphene was calculated. These calculations pinpoint Ni_4 as an interesting candidate to enhance the spin properties of the Ni_n/graphene system. Firstly, the Dirac cone is almost undistorted, preserving graphene's high carrier mobilities. Secondly, the Ni_4 cluster has a large doping efficiency, implying a strong charge transfer to graphene. Finally, non-collinear spin-polarized calculations of the Ni_4/graphene system indicate that the Ni_4 cluster gives rise to sizable spin splitting of the Dirac bands due to the induced spin–orbit coupling and exchange interaction.

To investigate the impact of the magnetic clusters on (spin) transport, a graphene spin valve is decorated with Ni_4 clusters at a density of 5.7×10^{12} clusters per cm^2. Following the example by Zomer *et al.*,[20] we study the spin relaxation mechanism by characterizing the spin transport parameters at different values of applied backgate voltages before and after cluster deposition. As the spin scattering mechanism in pristine graphene (*i.e.* the virgin state) is debated in the literature,[4] only a comparative study can unambiguously corroborate the contribution of the added scatterers. By performing Hanle spin precession measurements at different applied backgate

[a]*Quantum Solid-State Physics, Department of Physics and Astronomy, KU Leuven, Celestijnenlaan 200D, B-3001 Leuven, Belgium. E-mail: ewald.janssens@kuleuven.be, joris.vandevondel@kuleuven.be*
[b]*Semiconductor Physics Laboratory, Department of Physics and Astronomy, KU Leuven, Celestijnenlaan 200D, Leuven, B-3001, Belgium*
[c]*IMEC, Kapeldreef 75, Leuven, B-3001, Belgium*

† Electronic supplementary information (ESI) available. See DOI: https://doi.org/10.1039/d4nr01478b

voltages, the spin scattering time, τ_s, and the momentum scattering time, τ_p, are obtained. By comparing the 'before' and 'after' states of the device, the induced effects of the clusters are identified as an Elliot–Yafet (EY) like spin scattering mechanism.

2 DFT calculations of Ni_n/graphene

First-principles calculations were performed using the Vienna *ab initio* simulation package (VASP) with plane wave basis sets and projected-augmented wave (PAW) potentials.[21–23] First, the ground state geometrical configurations of the Ni_n clusters adsorbed on graphene were obtained by performing simulations with non-local vdW-DF2 exchange and correlation functionals.[24,25] The clusters were placed at different possible adsorption sites in the 5 × 5 graphene supercell with an interlayer spacing of 20 Å. This corresponds to a cluster density of 7.6×10^{13} cm^{-2}. The systems were relaxed until the forces between the atoms were less than 25 meV $Å^{-1}$ using a 5 × 5 × 1 *k*-point mesh with an energy cutoff of 520 eV. Furthermore, electronic structure calculations were performed on a denser mesh of 11 × 11 × 1 *k*-points. For Ni_3 and Ni_5 adsorbed on graphene, the Ni d-states are close to the Dirac point, resulting in a distortion of the Dirac cone in the spin-polarised band structure. As discussed below, the Ni_4 cluster preserves the Dirac cone and thus the high carrier mobility, while it has at the same time a large doping efficiency per cluster, implying a stronger charge transfer to graphene, with a high mobility and strong localized magnetic moment. Therefore, we direct our attention to Ni_4 clusters as a test bed to explore the physics at play when magnetic clusters are adsorbed on graphene.

The resultant total energies were compared to obtain the most stable configuration, which is shown in Fig. 1(a). The isolated Ni_4 cluster is tetrahedrally shaped and it prefers to adsorb with a single Ni atom on the bridge position (between two carbon atoms) with bond lengths of 2.119 Å and 2.299 Å. The Ni_4 adsorption energy is calculated to be −1.05 eV, indicating a stronger interaction than physisorption (a few hundred meV), but too weak for a real chemical bond. It can be seen from electronic structure calculations that Ni_4 donates electrons to graphene, resulting in a (Ni^+C^-) charge state type of attraction at the adsorption site. The adsorption of the Ni_4 cluster leads to the elongation of the C–C bond length by ~0.01 Å. The adsorbed Ni_4 has a localised magnetic moment of $3.3\mu_B$, which is slightly reduced when compared to the magnetic moment of the isolated cluster ($3.7\mu_B$).

The doping characteristics of the cluster are studied by performing open-shell electronic structure calculations. From the band structure of the Ni_4/graphene system, the Dirac cone is almost undistorted (see Fig. 1(b)) and the adsorption of the Ni_4 cluster preserves the high carrier mobility of graphene. The resultant band structure yields an n-type doping, as can be observed from the apparent shift of the Dirac cone below the Fermi level, which is consistent with the experimental results that are presented in section 3. From the shift of the Dirac point, one can compute the charge carrier doping density,[26] which corresponds to a doping efficiency of about 0.09 electrons per cluster. While the electron transfer was found to be independent of the supercell size, its absolute value does vary slightly with the size of the supercell (see the ESI† for details).

In the next step, we studied the induced spin-dependent effects of the Ni_4 cluster on the graphene layer. The induced spin splitting is estimated from the band splitting along the graphene band lines (*i.e.*, only the C-projected band states are considered) around the Dirac point. The band gap amounts to 25 meV and the obtained values of the band line splitting vary

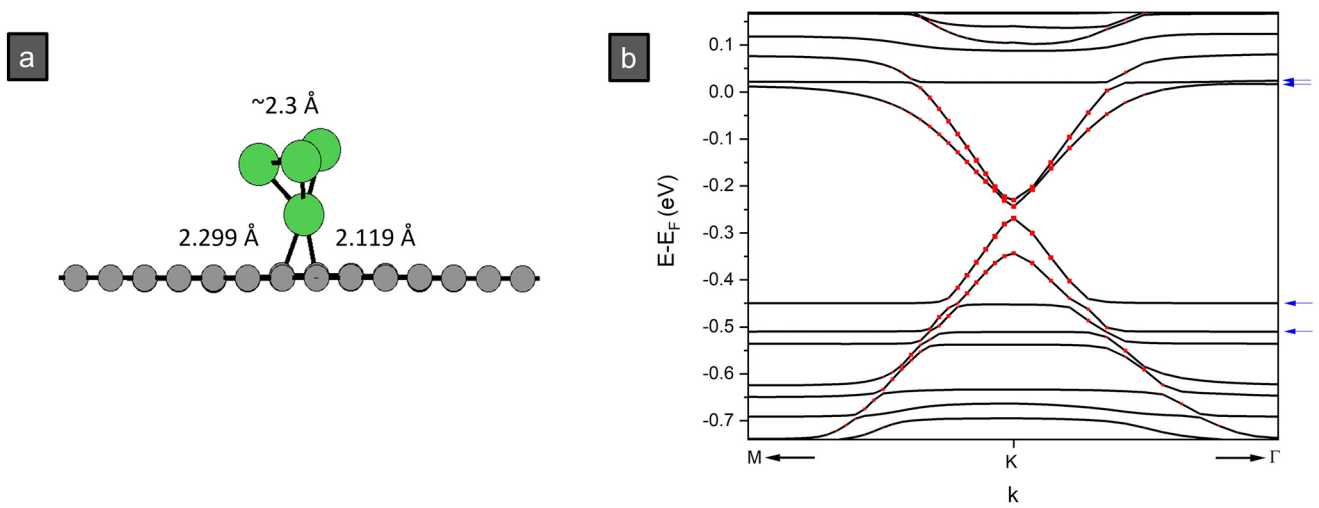

Fig. 1 (a) The optimized geometrical structure obtained for Ni_4/graphene after relaxation. (b) Non-collinear band structure of the Ni_4/graphene system, where the red-colored dots represent the C-projected bands. The band structure is zoomed close to the Dirac point around the symmetry point *K*. The blue arrows mark the 4 Ni states, located close to the band extrema, which were used in the tight binding Hamiltonian.

along the M → K → Γ path with an average value of 48.5 meV for the valence band and 29.9 meV for the conduction band. These values vary slightly with the size of the supercell that is used in the computations, as discussed in the ESI.† The average value is computed by calculating the absolute energy difference between the spin-split C-projected band in the −0.6 eV to 0 eV energy range. The origin of the induced spin-splitting is discussed below.

To qualitatively study the strength of different SOC terms, we constructed a tight binding Hamiltonian model to reproduce the electronic structure of the Ni_4/graphene system close to the Dirac point. From the DFT band structure, four Ni states are located close to the band extrema. These states are indicated by blue arrows in Fig. 1(b). A simple model was constructed dealing only with the interaction between the Ni anchor atom (with four spin states) and the two graphene C atoms (with two spin states per site). The Hamiltonian is given by

$$\begin{aligned} H = {} & \varepsilon_0 \sum_{i=m,n,\neq \mathrm{ads},\mathrm{ads}_{NN}} c_{i\sigma}^{+} c_{i\sigma} \\ & + t \sum_{i=m,n} c_{i\sigma}^{+} c_{i\sigma} + t_{\mathrm{C-Ni}} \sum_{i=\mathrm{ads}_{1,2}} c_{i\sigma}^{+} h_{M\sigma} \\ & + \sum_{M} (\varepsilon_{\mathrm{Ni}} - J_{\mathrm{Ni}}) h_{M\sigma}^{+} h_{M\sigma} + \sum_{i=\mathrm{ads}_1} (\varepsilon_{\mathrm{ads}_1} - J_1 \sigma_z) c_{i\sigma}^{+} c_{i\sigma} \\ & + \sum_{i=\mathrm{ads}_2} (\varepsilon_{\mathrm{ads}_2} - J_2 \sigma_z) c_{i\sigma}^{+} c_{i\sigma} + H_{\mathrm{SO}} \end{aligned} \tag{1}$$

Here, $c_{i\sigma}^{+}(c_{i\sigma})$ and $h_{M\sigma}^{+}(h_{M\sigma})$ correspond to the creation (annihilation) operator for an electron with spin σ at graphene lattice site i and cluster site M, respectively. ε_0 and t represent on-site and nearest-neighbor hopping energies between the carbon atoms. The onsite energy and local Zeeman coupling of the Ni atom are given by $\varepsilon_{\mathrm{Ni}}$ and J_{Ni} respectively. The adsorption of the Ni cluster modifies the onsite potential ($\varepsilon_{\mathrm{ads}_1}$) and induces a local magnetic interaction (J_1) at the closest (2.119 Å) adsorption site and its two nearest neighboring sites. J_2 corresponds to the Zeeman coupling at the carbon site 2.299 Å from the Ni_4 cluster. This C site is the third nearest neighbor of the closest adsorption site, but due to the bonding with the Ni atom, the on-site potential ($\varepsilon_{\mathrm{ads}_2}$) is slightly modified. The hopping from C to Ni ($t_{\mathrm{C-Ni}}$) was set to 0.5 eV to fit the DFT band structure. The spin–orbit coupling Hamiltonian is derived based on ref. 27–29 as follows:

$$\begin{aligned} H_{\mathrm{SO}} = {} & \frac{i}{3\sqrt{3}} \sum_{i=\langle\langle \mathrm{ads}_{1,2} \rangle\rangle,\sigma\sigma'} c_m^{\dagger} c_{n\sigma'} (\lambda_i + \xi_i \lambda_{\mathrm{VZ}}) [\vec{\sigma}]_{\sigma\sigma'} \cdot [\vec{S}_z]_{\sigma\sigma'} \\ & + \frac{2i}{3} \sum_{i=\langle \mathrm{ads}_{1,2} \rangle,\sigma\sigma'} c_m^{\dagger} c_{n\sigma'} \lambda_{\mathrm{BR}} (\hat{s} \times \vec{d}_{mn})_{z,\sigma\sigma'} \\ & + \frac{2i}{3} \sum_{i=\langle \mathrm{ads}_{1,2} \rangle,\sigma\sigma'} c_i^{\dagger} c_{i\sigma'} \xi_i \lambda_{\mathrm{PIA}}^{\mathrm{A/B}} (\hat{s} \times \vec{D}_{mn})_{z,\sigma\sigma'} \end{aligned} \tag{2}$$

The first term represents spin-conserving next nearest neighbor hopping, with the intrinsic (λ_i) and valley-Zeeman (λ_{VZ}) spin–orbit terms, where $\lambda_i = \frac{\lambda_i^{\mathrm{A}} + \lambda_i^{\mathrm{B}}}{2}$ and $\lambda_{\mathrm{VZ}} = \frac{\lambda_i^{\mathrm{A}} - \lambda_i^{\mathrm{B}}}{2}$. The second term in eqn (2) represents the spin mixing nearest neighbor hopping, with λ_{BR} being the Bychkov–Rashba spin–orbit coupling term. The third term in eqn (2) corresponds to the spin mixing next nearest neighbor hopping, where $\lambda_{\mathrm{PIA}}^{\mathrm{A/B}}$ is the strength of the pseudospin inversion asymmetry induced spin–orbit coupling, due to the sublattice symmetry breaking. In the above Hamiltonian, ξ_i is +1 (−1) for sublattice A (B), υ_{mn} is +1 (−1) for the clockwise (counterclockwise) hopping path to the next nearest neighbor site, and d_{mn} (D_{mn}) is the unit vector from site n to its nearest (next-nearest) site m. The single (double) bracket represents the sum of the first (second) nearest neighbor sites.

The tight binding model was fitted to the spin-split conduction and valence Dirac cones of the Ni_4/graphene system. The parameters were obtained by minimizing the energy difference in the DFT computed band lines and are provided in Table 1. The strength of the SOC is given by the magnitude of λ, and its sign corresponds to the direction of the spin splitting. The calculated electronic band structure, obtained from the tight binding model, is compared with the DFT simulations in Fig. 2. The tight binding model reproduces the DFT spin–orbit band structure close to the Dirac point. The tight-binding analysis suggests that the spin conserving valley-Zeeman-type SOC, represented by a large value of λ_{VZ}, dominates the SOC interaction in the Ni_4/graphene system.

3 Experimental results

3.1 Device characteristics

The device used as a starting point to fabricate the Ni_4/graphene hybrid is presented in Fig. 3. A more in-depth discussion of the sample fabrication process can be found in ref. 17. The graphene layer resides on a highly doped Si substrate terminated with a 300 nm SiO_2 top layer. The graphene is grown using platinum-based chemical vapor deposition (Pt-CVD) and subsequently transferred to the substrate.[30] The graphene's area of interest lies between the two magnetic contacts indicated by the width (W) and length (L) of the probed area, both of which are 10 μm. A backgate voltage V_g can be applied between the highly doped Si electrode and the graphene channel. To ensure a difference in magnetization reversal of the two Co electrodes at the center, the widths of these Co bars are set at 290 nm and 320 nm, respectively. The interface between these Co electrodes and graphene is made of 1 nm TiO_x to facilitate the spin injection and measurement. These left and right barriers behave as ohmic contacts in the applied voltage range and are roughly 425 Ω and 280 Ω, respectively. Conductivity measurements are performed by applying a current from #1 to #4 while measuring voltage over #2 and #3. Nonlocal measurements, *i.e.* the Hanle spin precession measurement, are carried out by applying a current from #2 to #1, while a nonlocal voltage is measured over #4 and #3. Both the conductivity and non-local transport measurements are performed at room temperature and a current of 10 μA is used. For such a low current, the effect of heating in these graphene devices can be ignored.[31] During the Hanle spin precession

Table 1 Tight binding parameters used to reproduce the DFT SO band structure of the Ni_4/graphene system. The two values for ε_{Ni} and J_{Ni} are due to the consideration of only two sites for the Ni anchor atom in the model

Orbital parameters (eV)							
ε_0	t	ε_{ads_1}	ε_{ads_2}	ε_{Ni}	J_{Ni}	J_1	J_2
−2.16	−2.53	−5.94	−6.82	−2.79, −2.30	0.030, 0.023	−0.056	0.082
Spin–orbit parameters (meV)							
λ_i	λ_{VZ}	λ_{BR}	λ^A_{PIA}	λ^B_{PIA}			
16.9	−59.8	4.22	1.60	−8.06			

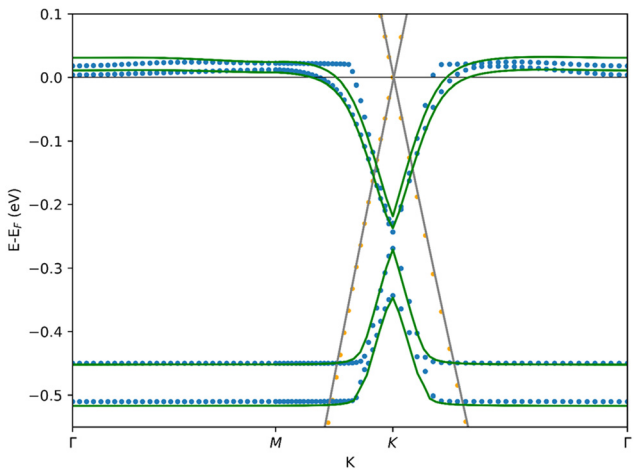

Fig. 2 The band extrema of the Ni_4/graphene system obtained with the simple tight binding Hamiltonian (solid green line) in comparison with the DFT SO band structure (blue dots). The band extrema of pristine graphene computed using DFT (orange dots) and a simple tight binding Hamiltonian (solid grey line) are shown for reference purposes. Tight binding computations are done using a hopping parameter of −2.5 eV and a spin orbit coupling strength of 12 μeV.

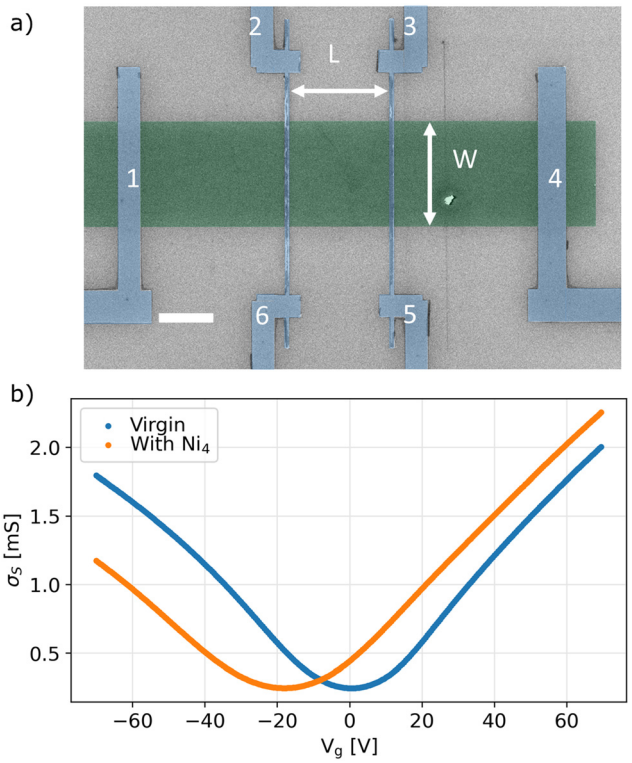

Fig. 3 (a) Scanning electron micrograph of the device. The scalebar represents 5 μm. The Co/TiO_x electrodes (false coloured in blue) are numbered #1–#6. The horizontal dark strip is the graphene flake (false coloured in green). (b) Sheet conductivity σ_S of graphene as a function of backgate voltage V_g of the virgin and Ni_4 decorated device.

measurements, after aligning the magnetization of the central Co electrodes, a magnetic field is applied perpendicular to the plane of the graphene. The measurements are done for field strengths ranging from −120 mT to +120 mT.

Using a magnetron sputtering gas aggregation cluster source,[32] a molecular beam of nickel clusters is formed. Ni_4^+ clusters are selected with atomic precision using a quadrupole mass filter and finally soft-landed on graphene devices. With a retarding field, the average kinetic energy of the Ni_4^+ clusters was determined to be 5.1 eV.[33] During deposition, the device was supplied a repelling voltage of +2.5 V, reducing the average landing energy of the clusters to 2.6 eV. Therefore, the cluster energy is tuned to the soft-landing regime (1 eV per atom (ref. 34)). The beam current I_B was recorded during the deposition, and after integration, the total cluster density was found to be $n_c = 5.7 \times 10^{12}$ clusters per cm^2.

3.2 Impact of Ni_4 on charge transport properties

Fig. 3(b) presents the backgate dependent conductivity measurements of graphene in the virgin state and after Ni_4 cluster deposition. For the virgin state, these measurements indicate a charge neutrality point, V_{CNP}, of +0.5 V and an average mobility $\mu_{av} = (\mu_e + \mu_h)/2$ of 2.7×10^3 cm^2 V^{-1} s^{-1}. The electron and hole mobilities (μ_e and μ_h, respectively) are extracted from linear least-squares fitting procedures with a 2 V interval around the steepest part of the conductivity curve $\sigma_S(V_g)$.[35] The V_{CNP} becomes −18 V after cluster deposition. The shift of V_{CNP} corresponds to a doping efficiency of 0.15–0.25 electrons per Ni_4 cluster taking into account the 5.7×10^{12} clusters per cm^2 deposited density. The hole mobility after cluster deposition decreased to 1.9×10^3 cm^2 V^{-1} s^{-1}, while the electron mobility became 2.3×10^3 cm^2 V^{-1} s^{-1}. The different influence of the Ni_4 clusters on the electron and hole

mobilities, which is reflected in the enhanced asymmetry of the sheet conductivity curve after cluster deposition, can be attributed to the stronger Ni–graphene interaction in the hole Dirac cone than in the electron Dirac cone. This aligns with the calculated band structure (Fig. 1), where the energy difference of Ni states in the valence band with the Dirac point (~0.2 eV) is slightly smaller than the corresponding energy difference of Ni states in the conduction band. Compared to the cases of Au_3 and Au_6,[17] the results correspond to each other in a qualitative sense, where a decrease in mobility was seen as well following cluster deposition. However, quantitatively, the electron donation per cluster is larger than that of the Au_6 cluster by a factor of ~3 and almost two orders of magnitude compared to the Au_3 cluster. Considering the Pauling electronegativity of Au and Ni (2.4 and 1.8), compared to 2.5 for C, Ni has a lower tendency to attract electrons and it therefore donates more electrons to graphene. Compared to the simulations, the experimentally obtained doping efficiency is twice as large. This discrepancy could be due to the fact that DFT simulations are performed on ideal free-standing graphene monolayers, *i.e.* neither defects nor substrate effects are taken into account. Next, the spintronic properties of the device are evaluated, both in the virgin state and after Ni_4 deposition.

3.3 Spin transport characteristics of the virgin state

3.3.1 Hanle measurements and spin signal amplitude. Fig. 4(a) presents a selection of Hanle spin precession measurements performed at applied backgate voltages of V_g = −50 V, 0 V and 50 V. The background has been subtracted from the presented data (see the ESI of ref. 17 for details). It is clear that the amplitude of the nonlocal resistance ('Amp') is large at V_g = ±50 V, but low for the one performed around V_{CNP}. By extracting the amplitude for all Hanle curves at different applied backgate voltages by means of least squares fits (lines in panel (a)), the purple curve presented in panel (c) is obtained. It should be noted that the non-local resistance is lower at applied backgate voltages V_g close to V_{CNP}, which is around 0 V in the virgin state (see Fig. 3(b)). Combined with the linear $V(I)$ observed for all contacts, the gate dependence of the nonlocal spin signal indicates spin injection and detection dominated by pin-holes in the barriers.[36] The background observed in the nonlocal measurements, similar to the one observed by Volmer and co-workers,[37] corroborates the pin-hole nature of the barriers. These pin-holes could inject and detect the spin in a non-uniform way.

3.3.2 Spin transport parameters. The parameters extracted from the Hanle measurements are the conventional spin transport parameters, with the diffusion constant D and the spin lifetime τ_s. The graphene's V_g dependence on the fitted τ_s and D in the virgin state and after Ni_4 adsorption is presented in Fig. 5. Similar to the signal amplitude as a function of applied backgate voltage, the spin transport parameters show minima around $V_g \simeq V_{CNP}$. The relative $(1 - \sigma)$ error on these parameters ranges from 10% to 30%, with the largest error around the charge neutrality point, where the S/N ratio is lower due to the diminished signal amplitude. These errors are estimated from χ^2 analysis. As the signal degrades even further after cluster deposition, the error on these fitting parameters around V_{CNP} becomes too large and therefore, the measurements are omitted in panels 5(b) and 5(d).

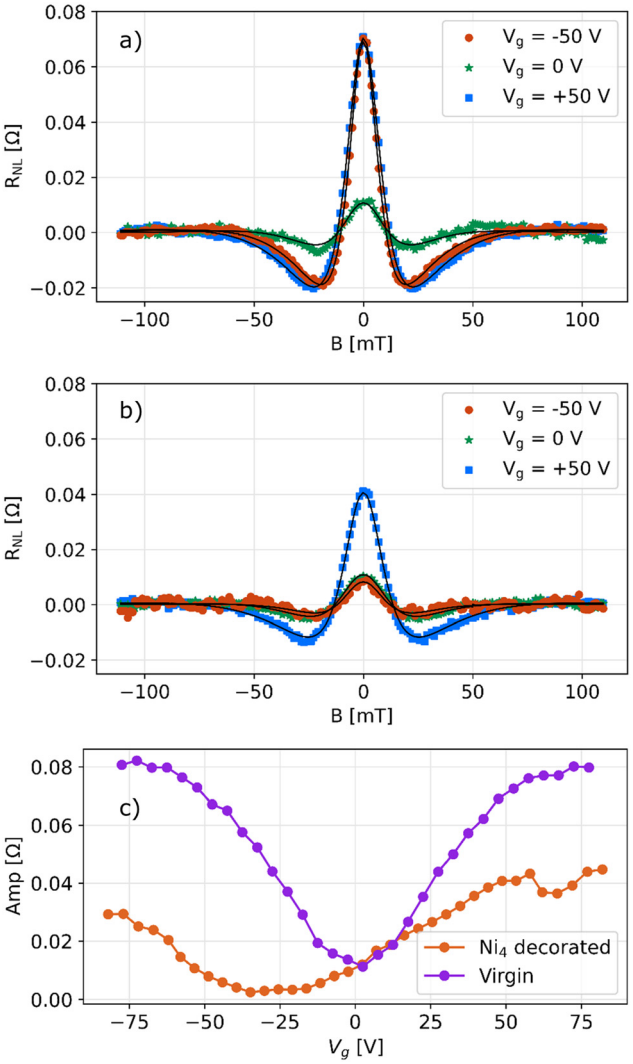

Fig. 4 (a) Hanle spin precession measurements, after background subtraction, at backgate voltages V_g = −50 V, 0 V and 50 V in the virgin state. (b) Repeat of the measurement in panel (a) after Ni_4 deposition. (c) Amplitude of the nonlocal resistance at zero field, after background subtraction, as a function of backgate voltage. All data are corrected for back-gate creep (see the ESI of ref. 17 for details).

Since the Elliot–Yafet (EY) and D'yakonov Perel (DP) mechanisms have very different dependencies on the Fermi level E_F and the momentum scattering lifetime τ_p, studying the spin transport parameters at different V_g values provides information about the scattering mechanism at play. As introduced by Zomer *et al.*,[20] the spin scattering rate can be written as Matthiessen's rule of summation of the scattering rates caused by EY and DP simultaneously: $\tau_s^{-1} = \tau_{s,EY}^{-1} + \tau_{s,DP}^{-1}$, assuming that individual scattering probabilities are independent of each other. Inserting the formulas for EY and DP, with Δ_{EY} being the spin–orbit coupling strength of the EY interaction[38]

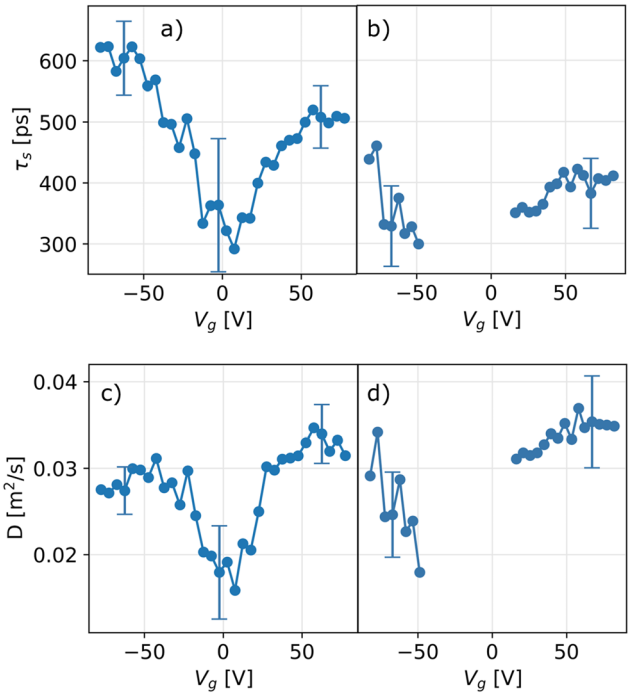

Fig. 5 Spin transport parameters of the graphene spin valve. (a) Spin lifetime τ_s and (c) diffusion constant D as a function of V_g for the device in the virgin state. (b) Spin lifetime τ_s and (d) diffusion constant D as a function of V_g for the device after Ni_4 deposition. All data shown are averaged for the gate up and down measurements after V_{CNP} creep correction.[17]

and Δ_{DP} being the spin–orbit coupling strength of the DP interaction,[39]

$$\tau_{s,EY}^{-1} = \frac{\Delta_{EY}^2}{E_F^2 \tau_p} \quad (3)$$

$$\tau_{s,DP}^{-1} = \frac{4\Delta_{DP}^2 \tau_p}{\hbar^2} \quad (4)$$

into Matthiessen's rule gives:

$$\frac{E_F^2 \tau_p}{\tau_s} = \Delta_{EY}^2 + \left(\frac{4\Delta_{DP}^2}{\hbar^2}\right)(E_F^2 \tau_p^2). \quad (5)$$

Fig. 6 presents the left hand side term, $\frac{E_F^2 \tau_p}{\tau_s}$, as a function of $E_F^2 \tau_p^2$. τ_s is directly obtained from the Hanle fit, E_F is measured from V_{CNP} and the applied gate voltage, and τ_p is calculated from the Hanle fit-parameter D using the relation $D = v_F^2 \tau_p/2$, where $v_F \approx 10^6$ m s^{-1}. Using this presentation of the data, eqn (5) implies that a linear fit estimates the slope as $4\Delta_{DP}^2/\hbar^2$ and the offset as Δ_{EY}^2. It should be noted that not all data extracted from the Hanle fit are presented here. Although the S/N ratio close to the V_{CNP} is still reasonable for the characterization of the virgin state, the signal decreased too much after deposition in order to obtain reliable fitting parameters. Therefore, for consistency, the data close to the V_{CNP} that could not be measured in the decorated state also was left out of the fit and figure in the virgin state.

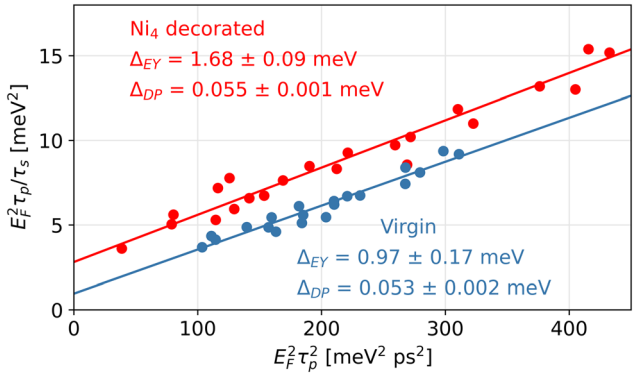

Fig. 6 Hanle fit parameters (τ_s and $\tau_p = 2D/v_F^2$) before and after Ni_4 cluster deposition presented according to eqn (5) as the blue and red circles for the virgin and Ni_4 decorated device, respectively. The offset and slope of the linear fits plotted are related to the Δ_{EY} and Δ_{DP} coupling strengths.

The linear fit performed on the virgin state measurement provides an EY SOC $\Delta_{EY} = 0.97 \pm 0.17$ meV and a DP SOC $\Delta_{DP} = 0.053 \pm 0.002$ meV. It can be seen from these values that both scattering mechanisms have a non-zero contribution to the total spin scattering. Compared to the exfoliated graphene samples measured in Zomer *et al.*,[20] where the EY coupling strength lies in a range of 1–2 meV and DP in a range of 0.05–0.1 meV, the experimental values obtained here are of similar magnitude. Graphene devices on a SiO_2 substrate also showed similar coupling strengths.[15] Using the EY and DP scattering strengths measured from the linear fit on the virgin state data (Fig. 6), the spin scattering rates of the two mechanisms can be compared directly. For example, at 50 V from the charge neutrality point ($E_F = 0.22$ eV), the scattering rate of DP is 1.5 ns^{-1}, while that of the EY mechanism is 0.35 ns^{-1}. While for the largest applied backgate voltages, $V_g = \pm 75$ V, corresponding to $|E_F| \approx 0.27$ eV, the DP induced scattering rate is almost an order of magnitude higher than the EY induced scattering rate. This difference in the spin scattering rate can be calculated from eqn (3) and (4) using the SOC obtained from the fit and a typical τ_p of 50 fs. Only when $|E_F| \lesssim 0.13$ eV ($V_g - V_{CNP} \lesssim 18$ V), the EY induced scattering rate is larger than the DP induced scattering rate. However, in contrast to the Fermi level regimes away from the Dirac point, where the measured τ_s (Fig. 5(a and b)) corresponds to the sum of both scattering mechanisms, this sum fails to capture the behaviour around the Dirac point. As the EY spin scattering rate is proportional to E_F^{-2}, the scattering rate tends to infinity as $E_F \to 0$. Thermal broadening and charge puddles are not taken into account in this formula, which could explain the discrepancy with the experimental data.

3.4 Spin transport characteristics of the Ni_4 cluster decorated state

3.4.1 Hanle measurements and spin signal amplitude. After performing the analysis on the virgin state of the graphene spin valve, the spin transport parameters of graphene

with a deposited density of 5.7×10^{12} Ni_4 clusters per cm^2 are examined. As discussed in section 3.2, the charge neutrality point shifts from +0.5 V to −18 V after Ni_4 cluster deposition (see Fig. 3(b)). Fig. 4(b) presents a few Hanle curves measured at different backgate voltages (−50 V, 0 V and 50 V). The amplitudes of the Hanle curves after deposition are smaller than those of the virgin sample. Moreover, since the V_{CNP} shifted to lower voltages after cluster deposition, the data measured at constant applied backgate voltages no longer have equal amounts of charge carriers due to the clusters acting as dopants. As such, the Hanle curves obtained at −50 V and 50 V are no longer identical. Considering Fig. 4(c), the V_g corresponding to minimum spin signal amplitude has shifted towards the new charge neutrality point.

3.4.2 Spin transport parameters. Fig. 6 presents the same analysis as was done for the virgin state of the device, but now for the decorated state shown as the red dots. Again, eqn (5) is used to extract the EY and DP SOC. The best fit parameters of the linear fit result in $\Delta_{EY} = 1.68 \pm 0.09$ meV and $\Delta_{DP} = 0.055 \pm 0.001$ meV. Comparing these coupling strengths with those in the virgin state, it is clear that the EY SOC increased significantly, while the DP SOC remains constant within the fit uncertainty. In summary, the backgate dependence of the spin transport parameters revealed a DP dominant spin relaxation mechanism in the virgin state away from the Dirac point. After the Ni_4 cluster deposition, an increase in the EY SOC coupling strength is found, while the DP SOC remained constant. This result indicates that the Ni_4 clusters introduced spin scattering *via* the EY mechanism. Next, the induced SOC by the Ni_4 clusters Δ_{EY,Ni_4} is further examined.

3.5 Ni_4 cluster-induced SOC in graphene

A comparison of the experimentally obtained SOC strengths with those found in the DFT calculations in section 2 requires isolating the Ni_4 contribution from the total coupling strength. We estimate the value for Δ_{EY,Ni_4}, representing the SOC strength associated with the Ni_4 clusters at certain backgate voltages. Two highly doped regimes are chosen: high p-doping and high n-doping, evaluated at $V_g - V_{CNP} = -50$ V and $V_g - V_{CNP} = +50$ V. In these high doping regimes, the spin lifetime could be extracted from the Hanle spin precession experiments with low uncertainty. The carrier densities in these regimes are $n = 3.59 \times 10^{12}$ holes per cm^2 and $n = 3.59 \times 10^{12}$ electrons per cm^2, respectively. In order to obtain Δ_{EY,Ni_4}, we consider eqn (6), representing the terms contributing to the total spin scattering rate:

$$\underbrace{\tau_s^{-1}}_{\text{spin scattering rate}} = \underbrace{\frac{\Delta_{EY,0}^2 \cdot \tau_{p,0}^{-1}}{E_F^2}}_{\text{virgin EY}} + \underbrace{\frac{\Delta_{EY,Ni_4}^2 \cdot \tau_{p,Ni_4}^{-1}}{E_F^2}}_{\text{cluster EY}} + \underbrace{4\left(\frac{\Delta_{DP}}{\hbar}\right)^2 \tau_p}_{\text{DP contribution}} \quad (6)$$

The first term on the right hand side represents the spin scattering contribution due to the virgin scatterers in the EY mechanism. The second term expresses the Ni_4 cluster EY scattering contribution. The last term represents the DP scattering contribution. The required data extracted from the measurements are collected in Table 2. Finally, inserting these quantities and their errors in the equations, the Ni_4 cluster induced SOC EY coupling strength is $\Delta_{EY,Ni_4} = 4.0 \pm 0.5$ meV evaluated at $V_g - V_{CNP} = -50$ V and $\Delta_{EY,Ni_4} = 4.3 \pm 0.5$ meV at $V_g - V_{CNP} = +50$ V (or −/+0.21 eV from the Dirac point, respectively).

For an intuitive way to understand eqn (6) and how the obtained Δ_{EY,Ni_4} relates to the Δ_{EY}, one has to consider the complete (spin) scattering picture of our device. When it scatters due to a scattering centre already present in the virgin sample there is about a 1 in 52 000 chance that the spin will scatter as well, since $\frac{\Delta_{EY,0}^2}{E_F^2} = \left(\frac{0.97\,\text{meV}}{0.221\,\text{eV}}\right)^2 = 1/52\,000$. When there is a momentum scattering event with the Ni_4 cluster, this probability is much higher: about 1 in 3000 as $\frac{\Delta_{EY,Ni_4}^2}{E_F^2} = \left(\frac{4.0\,\text{meV}}{0.221\,\text{eV}}\right)^2 = 1/3000$, with the coupling strength taken in the hole regime. In this picture, the Δ_{EY} provided by the linear regression in Fig. 6 can be regarded as the 'average' scattering probability behaving like the EY mechanism, weighted over the clusters and the other momentum scatterers. As seen in Table 2, the momentum lifetime decreases from $\tau_{p,0} = 53$ fs to $\tau_p = 43$ fs after Ni_4 deposition in the hole dominated regime and from $\tau_{p,0} = 58$ fs to $\tau_p = 50$ fs in the electron dominated regime. The relative contribution of the cluster momentum scatterers to the total momentum scattering equals $\tau_{p,Ni_4}^{-1}/\tau_p^{-1} = (\tau_p^{-1} - \tau_{p,0}^{-1})/\tau_p^{-1} = 19\%$ in the hole doped regime and 14% in the electron doped regime. This indicates that about 1 in 6 momentum scattering events are caused by the Ni_4 cluster. Therefore, the measured increase from $\Delta_{EY} = 0.97 \pm 0.17$ meV to $\Delta_{EY} = 1.68 \pm 0.09$ meV can be attributed to a Ni_4 EY coupling strength of $\Delta_{EY,Ni_4} = 4.0 \pm 0.5$ meV and $\Delta_{EY,Ni_4} = 4.3 \pm 0.5$ meV for the hole and electron charge carrier regimes, respectively.

Table 2 Overview of the spin and electronic transport properties, evaluated at the charge densities $n = 3.59 \times 10^{12}$ holes per cm^2 and $n = 3.59 \times 10^{12}$ electrons per cm^2. The momentum scattering time τ_p is found *via* the relation $\tau_p = \frac{h\sigma_s}{e^2 v_F \sqrt{4\pi n}}$ with $v_F \approx 10^6$ m s^{-1}

n_c	Virgin state	Ni_4 cluster decorated state
V_{CNP}	0.5 V	−18 V
n	3.59×10^{12} holes per cm^2	
E_F	−0.221 eV	
V_g	−49.5 V	−68 V
$\sigma_S(n)$	1.38 mS	1.13 mS
$\tau_p(\sigma_S,n)$	53 ± 1 fs	43 ± 1 fs
τ_s	560 ± 60 ps	330 ± 70 ps
n	3.59×10^{12} electrons per cm^2	
E_F	0.221 eV	
V_g	50.5 V	32 V
$\sigma_S(n)$	1.51 mS	1.30 mS
$\tau_p(\sigma_S,n)$	58 ± 1 fs	50 ± 1 fs
τ_s	500 ± 50 ps	360 ± 60 ps

The spin–orbit coupling strengths obtained from the tight binding model for the spin-mixing terms λ_{BR} and $\lambda_{PIA}^{A/B}$ (which act like a second-order Rashba SOC) are in close agreement with the experimental values obtained for Δ_{EY,Ni_4}. It should be noted that the presence of magnetic impurities can lead to an efficient spin relaxation mechanism due to resonant spin scattering induced by impurities, as shown by Kochan *et al.*[40] The presence of a larger spin–orbit coupling and exchange interaction induced by the adsorbed Ni_4 cluster could thus turn the clusters into local spin scatterers, which enhances the spin flip probability for each scattering event. Consequently, Ni_4 clusters act as charge and magnetic dopants in graphene, having a strong impact on its spin transport properties while possibly maintaining graphene's high charge carrier mobility due to the weak distortion of the Dirac cone induced by the adsorbed clusters.

4 Conclusions

We performed an in-depth analysis of Ni_4 clusters on graphene using both DFT calculations and spin transport experiments. Before and after deposition analysis reveals an EY-like spin scattering mechanism induced by the Ni_4 clusters with an EY SOC strength of $\Delta_{EY,Ni_4} = 4.0 \pm 0.5$ meV. The overall SOC can only be 'engineered' up to a maximum of 4.0 ± 0.5 meV due to the nature of the EY mechanism by decorating graphene with Ni_4 clusters. When the cluster density is increased, the contribution of the cluster to the total momentum scattering moves closer towards 100%. The experimental values obtained for Δ_{EY,Au_3} and Δ_{EY,Au_6} were 5.7 meV and 3.9 meV.[17] These values are comparable to the one obtained for Δ_{EY,Ni_4} in the current work and as such, the magnetic character of nickel cannot be pinpointed as a much stronger source of spin scattering. In order to increase the SOC, different sizes or elements need to be examined and the experimental protocol presented in this work is ideally suited for performing such studies.

Data availability

The data that support the findings of this study are available from corresponding author JVdV upon reasonable request.

Conflicts of interest

There are no conflicts to declare.

Acknowledgements

This work is supported by the Research Foundation-Flanders (FWO, Belgium), grant no. G0D5619N.

References

1 A. H. Castro Neto and F. Guinea, *Phys. Rev. Lett.*, 2009, **103**, 026804.
2 J. Katoch, *Synth. Met.*, 2015, **210**, 68–79.
3 G. Jian-Lei, W. Tian-Ru, G. Ming, B. Zhan-Bin, C. Lu, W. Xue-Feng, Q. Yu-Yuan and S. Feng-Qi, *Front. Phys.*, 2017, **12**, 127210.
4 B. Raes, J. E. Scheerder, M. V. Costache, F. Bonell, J. F. Sierra, J. Cuppens, J. Van De Vondel and S. O. Valenzuela, *Nat. Commun.*, 2016, **7**, 11444.
5 T. S. Ghiasi, J. Ingla-Aynés, A. A. Kaverzin and B. J. Van Wees, *Nano Lett.*, 2017, **17**, 7528–7532.
6 J. Bundesmann, D. Kochan, F. Tkatschenko, J. Fabian and K. Richter, *Phys. Rev. B: Condens. Matter Mater. Phys.*, 2015, **92**, 081403.
7 L. A. Benítez, J. F. Sierra, W. Savero Torres, A. Arrighi, F. Bonell, M. V. Costache and S. O. Valenzuela, *Nat. Phys.*, 2018, **14**, 303–308.
8 A. Ferreira, T. G. Rappoport, M. A. Cazalilla and A. H. Castro Neto, *Phys. Rev. Lett.*, 2014, **112**, 066601.
9 D. Van Tuan, J. M. Marmolejo-Tejada, X. Waintal, B. K. Nikolić, S. O. Valenzuela and S. Roche, *Phys. Rev. Lett.*, 2016, **117**, 176602.
10 Z. Jia, B. Yan, J. Niu, Q. Han, R. Zhu, D. Yu and X. Wu, *Phys. Rev. B: Condens. Matter Mater. Phys.*, 2015, **91**, 085411.
11 C. K. Safeer, J. Ingla-Aynés, F. Herling, J. H. Garcia, M. Vila, N. Ontoso, M. R. Calvo, S. Roche, L. E. Hueso and F. Casanova, *Nano Lett.*, 2019, **19**, 1074–1082.
12 P. Zhang and M. W. Wu, *New J. Phys.*, 2012, **14**, 033015.
13 A. G. Swartz, J. R. Chen, K. M. McCreary, P. M. Odenthal, W. Han and R. K. Kawakami, *Phys. Rev. B: Condens. Matter Mater. Phys.*, 2013, **87**, 20–23.
14 K. Pi, W. Han, K. M. McCreary, A. G. Swartz, Y. Li and R. K. Kawakami, *Phys. Rev. Lett.*, 2010, **104**, 187201.
15 C. Józsa, T. Maassen, M. Popinciuc, P. J. Zomer, A. Veligura, H. T. Jonkman and B. J. Van Wees, *Phys. Rev. B: Condens. Matter Mater. Phys.*, 2009, **80**, 1–4.
16 W. Han and R. K. Kawakami, *Phys. Rev. Lett.*, 2011, **107**, 047207.
17 W. Keijers, R. Murugesan, G. Libeert, J. E. Scheerder, B. Raes, S. Brems, S. D. Gendt, M. Houssa, E. Janssens and J. V. de Vondel, *J. Phys.: Mater.*, 2021, **4**, 045005.
18 S. E. Apsel, J. W. Emmert, J. Deng and L. A. Bloomfield, *Phys. Rev. Lett.*, 1996, **76**, 1441–1444.
19 R. Ambrusi, V. Orazi, J. Marchetti and M. Pronsato, *J. Phys. Chem. Solids*, 2020, **138**, 109258.
20 P. J. Zomer, M. H. D. Guimarães, N. Tombros and B. J. van Wees, *Phys. Rev. B: Condens. Matter Mater. Phys.*, 2012, **86**, 161416.
21 G. Kresse and J. Furthmüller, *Comput. Mater. Sci.*, 1996, **6**, 15–50.
22 G. Kresse and D. Joubert, *Phys. Rev. B: Condens. Matter Mater. Phys.*, 1999, **59**, 1758.
23 G. Kresse and J. Hafner, *Phys. Rev. B: Condens. Matter Mater. Phys.*, 1993, **47**, 558–561.

24 J. P. Perdew, K. Burke and M. Ernzerhof, *Phys. Rev. Lett.*, 1996, **77**, 3865.
25 K. Lee, É. D. Murray, L. Kong, B. I. Lundqvist and D. C. Langreth, *Phys. Rev. B: Condens. Matter Mater. Phys.*, 2010, **82**, 081101.
26 M. S. Lundstrom and C. Jeong, *Near-equilibrium transport: fundamentals and applications*, World Scientific Publishing Company, 2013, vol. 2, p. 252.
27 A. W. Cummings, J. H. Garcia, J. Fabian and S. Roche, *Phys. Rev. Lett.*, 2017, **119**, 206601.
28 M. Gmitra, D. Kochan and J. Fabian, *Phys. Rev. Lett.*, 2013, **110**, 246602.
29 K. Song, D. Soriano, A. W. Cummings, R. Robles, P. Ordejón and S. Roche, *Nano Lett.*, 2018, **18**, 2033–2039.
30 K. Verguts, Y. Defossez, A. Leonhardt, J. D. Messemaeker, K. Schouteden, C. V. Haesendonck, C. Huyghebaert, S. D. Gendt and S. Brems, *ECS J. Solid State Sci. Technol.*, 2018, **7**, 195–200.
31 G. Libeert, R. Murugesan, M. Guba, W. Keijers, S. Collienne, B. Raes, S. Brems, S. De Gendt, A. V. Silhanek, T. Höltzl, M. Houssa, J. Van de Vondel and E. Janssens, *Nanoscale*, 2022, **14**, 12437–12446.
32 Z. Li, H.-Y. T. Chen, K. Schouteden, T. Picot, K. Houben, T.-W. Liao, C. Van Haesendonck, G. Pacchioni, P. Lievens and E. Janssens, *Nano Lett.*, 2016, **16**, 3063–3070.
33 J. E. Scheerder, T. Picot, N. Reckinger, T. Sneyder, V. S. Zharinov, J.-F. Colomer, E. Janssens and J. Van de Vondel, *Nanoscale*, 2017, **9**, 10494–10501.
34 S. R. Plant, L. Cao, F. Yin, Z. W. Wang and R. E. Palmer, *Nanoscale*, 2014, **6**, 1258–1263.
35 J. H. Chen, C. Jang, S. Adam, M. S. Fuhrer, E. D. Williams and M. Ishigami, *Nat. Phys.*, 2008, **4**, 377–381.
36 W. Han, K. Pi, K. M. McCreary, Y. Li, J. J. I. Wong, A. G. Swartz and R. K. Kawakami, *Phys. Rev. Lett.*, 2010, **105**, 3–6.
37 F. Volmer, M. Drögeler, T. Pohlmann, G. Güntherodt, C. Stampfer and B. Beschoten, *2D Mater.*, 2015, **2**, 024001.
38 H. Ochoa, A. H. Castro Neto and F. Guinea, *Phys. Rev. Lett.*, 2012, **108**, 206808.
39 M. D'Yakonov and V. Perel', *Soviet J. Exp. Theor. Phys.*, 1971, **33**, 1053.
40 D. Kochan, M. Gmitra and J. Fabian, *Phys. Rev. Lett.*, 2014, **112**, 116602.